



Temperature dependent optical dispersion and electronic transitions of highly *a*-axis oriented $0.8\text{Pb}(\text{Zn}_{1/3}\text{Nb}_{2/3})\text{O}_3\text{-}0.2\text{PbTiO}_3$ films on SrTiO_3 crystals: An ellipsometric evidence



C.Q. Li, J.Z. Zhang, L.P. Xu, J.J. Zhu, Z.H. Duan, Z.G. Hu*, J.H. Chu

Department of Electronic Engineering, East China Normal University, Shanghai 200241, China

ARTICLE INFO

Article history:

Received 4 August 2015

Received in revised form 28 December 2015

Accepted 20 January 2016

Available online 25 January 2016

Keywords:

Relaxor ferroelectrics

Thin films

Optical dispersion

Phase transition

Band gap

ABSTRACT

The relaxor ferroelectric $0.8\text{Pb}(\text{Zn}_{1/3}\text{Nb}_{2/3})\text{O}_3\text{-}0.2\text{PbTiO}_3$ (0.8PZN-0.2PT) films have been fabricated on (100) SrTiO_3 substrates by the sol–gel method. The structure, optical properties and electronic transitions have been investigated using X-ray diffraction (XRD), atomic force microscopy, scanning electron microscopy and ellipsometric spectra. The pure perovskite phase with highly *a*-axis (100)-preferential orientation as well as low screw dislocation are extracted based on high resolution XRD. Moreover, the red-shift trend of the electronic transitions at about 3.01 eV as a function of temperature follows the Bose-Einstein law induced by the electron–phonon interactions and lattice thermal expansion. Interestingly, the different optical behavior and structure variation can be observed at about 500 K, which reveal tetragonal to cubic structural transformations for the 0.8PZN-0.2PT films. It indicates that the potential application of ellipsometric spectra in judging the phase transitions and symmetries of ferroelectric material.

© 2016 Elsevier B.V. All rights reserved.

1. Introduction

Relaxor ferroelectric materials, which are characterized by ferroelectric, pyroelectric and piezoelectric properties, have recently attracted tremendous attention as a candidate class of materials for use in the fields of electro-optic modulators, sensors, pyroelectric detectors, dynamic random access memories and microelectromechanical systems [1–4]. Pb-based perovskite relaxors with $A(\text{B}_i\text{B}_{ii})\text{O}_3$ structure are derived from the stereochemical activity of Pb [5], where A site ions are Pb ions and B sites consist of two different ions. The Pb off shifts primarily affect the occurrence of spontaneous polarization. The B-site order plays an important role in phase transition, dielectric response and interband electronic transitions. Pb-site-O and B-site-O hybridizations are essential in competing structural and polar instabilities of ferroelectrics, indicating the complexity of physical mechanism [6,7]. Lead zinc niobate $\text{Pb}(\text{Zn}_{1/3}\text{Nb}_{2/3})\text{O}_3$ (PZN) and lead titanate PbTiO_3 (PT) can form a complete solid solution $(1-x)\text{Pb}(\text{Zn}_{1/3}\text{Nb}_{2/3})\text{O}_3\text{-}x\text{PbTiO}_3$ (PZN-*x*PT), which is of a typical $A(\text{B}_i\text{B}_{ii})\text{O}_3$ structure. B-sites are occupied by Zn and Nb ions, while the combinations of Zn and Nb ions must be satisfied with the external effective chemical valency of +4 [8]. Correspondingly, the structural sort, which is related to physical properties, can be determined by doping or mixing the congeneric elements. The

phase diagram of PZN-*x*PT presents the information: for $x \leq 0.08$, the crystals show rhombohedral symmetry and the morphotropic phase boundary (MPB) corresponds to $x = 0.08\text{--}0.10$, whereas for $x > 0.1$, crystals exhibit tetragonal–cubic phase transition around 500 K and possess remarkable relaxor ferroelectric character [9,10].

In PZN-*x*PT systems, PZN-*x*PT crystals have received increasing attention not only due to their high dielectric permittivity, an extraordinary large piezoelectric strain (>6%), piezoelectric constant ($d_{33} > 2500$ pC/N), and high electromechanical coupling factor ($k_{33} > 0.9$) [11–15], but also to the outstanding optical performance, such as photorefractive, Second-Harmonic Generation (SHG), electro-optic and elasto-optical properties [16]. Optical materials, which are corresponding to electronic band structures with high electro-optic (EO) response, are widely used in modulators, EO deflectors, switches and filters [17]. Moreover, PZN-*x*PT films can integrate more easily with silicon, which makes PZN-*x*PT films the most promising materials as designing optical communication system and other optoelectronic devices for future equipment applications. Therefore, it is necessary to investigate the film preparation and physical properties. Several methods have been used to prepare PZN-*x*PT thin films, such as the sol–gel technique, pulsed laser deposition (PLD) and liquid phase epitaxy (LPE). Although we reported peculiar ferroelectric and dielectric properties for the PZN-*x*PT films at room temperature [18], the optical performance, such as the dielectric functions and electronic band structures at high temperature has not been done. Generally, ellipsometric spectroscopy can be used to obtain dielectric functions, optical band gap

* Corresponding author.

E-mail address: zg hu@ee.ecnu.edu.cn (Z.G. Hu).

E_g , absorption characteristics, and band tail state behavior by fitting the experimental data with a reasonable dispersion model. The fitting statistics mainly depend on the reliability of the inverse synthesis and the validity of the optical model. Therefore, one can take advantage of solid state spectroscopy to further excavate optical properties of PZN-xPT system.

In this work, we prepared 0.8PZN-0.2PT films on SrTiO₃ (STO) substrates using the sol-gel method. Temperature dependent dielectric functions and structural phase transitions of PZN-0.2PT films were studied in the infrared-ultraviolet range by spectroscopic ellipsometry. The corresponding band to band transitions have been discussed together with the structure variation.

2. Experimental details

2.1. Fabrication of 0.8PZN-0.2PT precursor solution and films

Before fabricating the 0.8PZN-0.2PT films on STO substrates, the precursor solution was synthesized using lead acetate trihydrate [Pb(CH₃COO)₂·3 H₂O], zinc acetate dihydrate [Zn(CH₃COO)₂·2 H₂O], niobium ethoxide [Nb(OC₂H₅)₅] and tetrabutyl titanate [(C₄H₉O)₄Ti] as starting materials. Pb(CH₃COO)₂·3 H₂O was dissolved fully in 2-methoxyethanol, and refluxed 40 min at 100 °C. Then the temperature was elevated to 128 °C for 20 min to remove the water of crystallization. After cooling down to room temperature, the required acetylacetone (CH₃COCH₂COCH₃), (C₄H₉O)₄Ti, Nb(OC₂H₅)₅ and Zn(CH₃COO)₂·2 H₂O were added to the solution orderly. Note that a small amount of the water of crystallization from Zn(CH₃COO)₂·2 H₂O cannot affect the solubility of the Nb(OC₂H₅)₅. The purpose of adding the CH₃COCH₂COCH₃ was to keep the precursor solution stable. Note that 6% excess lead was added to the solution for compensating any lead loss during the annealing process and promoting the formation of perovskite phase for the films. The final solution was adjusted to 0.2 M. The STO crystals were rigorously single-side polished and cleaned in pure ethanol with an ultrasonic bath and rinsed several times by deionized water. Finally, the 0.8PZN-0.2PT films were prepared on STO substrates by spinning coating process with a speed of 4000 rpm for 20 s. The deposited films were preheated at 200 °C for 5 min, 400 °C for 5 min, and 600 °C for 8 min, respectively. The required film thickness (about 200 nm) was obtained by repeating the above step for 10 times. The whole preparation of the precursor solution, spinning and thermal annealing process were performed in ambient atmosphere. The whole detailed process for preparing the precursor solution and 0.8PZN-PT films was depicted in Fig. 1.

2.2. XRD, AFM, SEM, XPS, and SE measurements

The crystallization, surface morphology and cross-section microstructure of the 0.8PZN-0.2PT films were characterized using X-ray diffraction (XRD, D/MAX-2550V, Rigaku Co.), atomic force microscopy (AFM, Digital Instruments Dimension 3100, Veeco) and a scanning electron microscope (SEM, Hitachi S-4800). X-ray photoelectron spectroscopy (XPS) experiments were carried out on a RBD upgraded PHI-5000C ESCA system (Perkin-Elmer) with Mg K α radiation ($h\nu = 1253.6$ eV). Temperature dependent ellipsometric experiments of the STO substrates and 0.8PZN-0.2PT films were carried out by a vertical variable-angle near-infrared-ultraviolet spectroscopic ellipsometry (SE, J.A. Woollam Co., Inc.) with an incident angle of 70° and the photon energy range of 1.1–5 eV (248–1100 nm). The films and STO samples were installed into an Instec cell with liquid nitrogen cooling accessory. The temperature range can be varied from 200 to 600 K with the precision of about ± 1 K. The window effect can be eliminated through the calibration of silicon sample. The system was continuously purged with dry N₂ not only to protect the sample surface from contamination but also to avoid water vapor in the ambient.

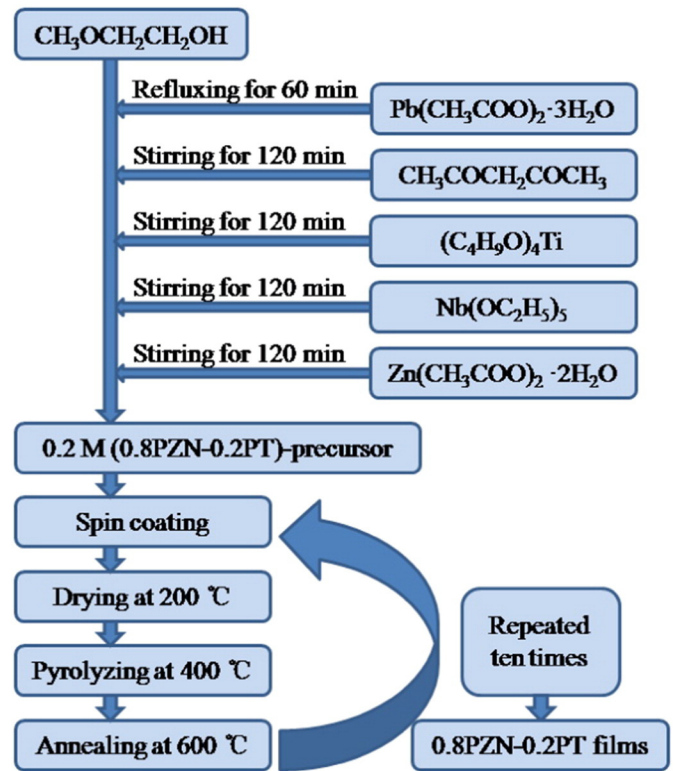


Fig. 1. Preparation process of the precursor and films for 0.8PZN-0.2PT.

3. Results and discussions

3.1. Structure analysis

Fig. 2(a) presents the XRD pattern of the 0.8PZN-0.2PT films annealed at 600 °C. No impurity phase is observed and only ($h00$) diffraction peak appears, which indicates that the preferential orientation of the 0.8PZN-0.2PT films is along the a -axis perpendicular to the substrate surface. As can be seen from the inset 1 of Fig. 2, the full width at half-maximum (FWHM) of the (100) peak is about 0.235°. From the FWHM of the (100) peak, the crystalline size of the samples is about 33 nm estimated by the Scherrer formula [$D = 0.89\lambda / (\beta \cos\theta)$]. Note that the insets 2 and 3 of Fig. 2 show the rocking curves of 0.8PZN-0.2PT films and STO substrates for the (100) peak, which were measured by high resolution X-ray diffraction. The FWHM of 0.8PZN-0.2PT films is 0.056°, which is closer to that of the STO substrates (0.046°). It suggests that the 0.8PZN-0.2PT films have remarkably low screw dislocation density and high structural perfection. The above data indicate that the 0.8PZN-0.2PT films are of good crystallinity. Generally, the choice of using the STO substrates is based on the small lattice mismatch and the large difference in the refractive index between the films and the STO substrates [19]. The STO crystal has a lattice constant of 3.905 Å, which is close to that of 0.8PZN-0.2PT films (4.02 Å) and 0.91Pb(Zn_{1/3}Nb_{2/3})O₃-0.09PbTiO₃ single crystals (4.03 Å) [18,20]. A smaller lattice mismatch between the films and substrates increases the growth periodic structure alternately. At the same photon energy of 2.5 eV, the refractive index of 0.8PZN-0.2PT films is 2.667, which is larger than that of STO (2.392) at room temperature. A larger refractive index difference between the films and substrates increases the amplitude of oscillations of ellipsometric spectra, and thus enhances the accuracy of ellipsometric measurements. Fig. 2(b) shows the AFM surface morphology of 0.8PZN-0.2PT films. One can find that each grain of the films is closely gathered layer after layer and the root-mean-square roughness of the surface is estimated to be about 5.23 nm, which is approximately 2.62% of the film thickness. From the cross sectional

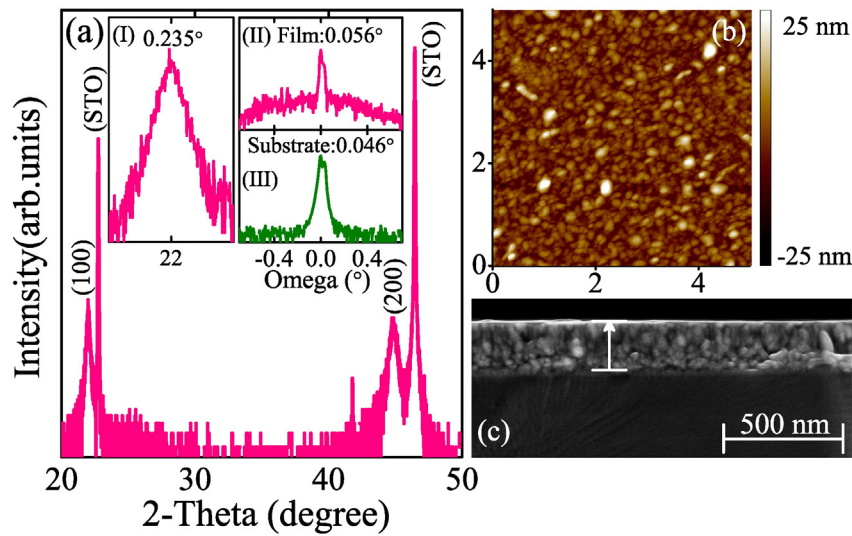


Fig. 2. (a) The XRD pattern of the 0.8PZN-0.2PT films on the STO substrates. The inset I shows the FWHM of the (100) diffraction peak and the insets II and III show the FWHM of the rocking curves for 0.8PZN-0.2PT films and substrates around the (100) peak, respectively. (b) AFM surface morphology and (c) cross-sectional SEM image of the 0.8PZN-0.2PT films.

structure of the 0.8PZN-0.2PT films (Fig. 2(c)), the thickness is estimated to be about 200 nm, which agrees well with the nominal value.

3.2. XPS of the 0.8PZN-0.2PT films

Chemical compositions and chemical states of the 0.8PZN-0.2PT films were studied by XPS measurements. The survey spectra of the samples show that only C 1s, Pb 4f, Zn 2p, Nb 3d, Ti 2p, and O 1s related core levels can be detectable. The C 1s peak at 284.6 eV is used as an internal standard and the other elemental spectra are calibrated with the C 1s peak to correct the binding energy position. Fig. 3(a) displays the overall core level XPS survey spectra of the 0.8PZN-0.2PT film. To obtain the separate information of each element, the XPS experimental data were fitted using Lorentzian–Gaussian functions. As an example, high-resolution spectra of Pb 4f, Zn 2p, Nb 3d, Ti 2p, and O 1s for the

0.8PZN-0.2PT film are presented in Fig. 3(b) and (f). The Pb 4f XPS spectrum of 0.8PZN-0.2PT was observed at 138.2 and 143.2 eV for 4f_{7/2} and 4f_{5/2} peak, which indicate that the Pb ion is of the +2 valence state. The Zn 2p XPS spectra of 0.8PZN-0.2PT were observed at 1021.6 eV for the 2p_{3/2} peaks in Fig. 3(c). The Nb 3d XPS spectrum of 0.8PZN-0.2PT was observed at 206.8 and 209.4 eV for 3d_{5/2} and 3d_{3/2} peak in Fig. 3(d). The Ti 2p XPS spectra of 0.8PZN-0.2PT were observed at 458.6 and 463.8 eV for the 2p_{3/2} and 2p_{1/2} peaks, respectively, as shown in Fig. 3(e). The XPS data suggest that the Ti ion is of the +4 valence state and the Zn ion is of the +2 valence state. In addition, the O 1s XPS spectra for the 0.8PZN-0.2PT film are fitted by two peaks, as can be seen in Fig. 3(f). One of the O 1s peaks located at 529.4 eV is ascribed to the lattice oxygen of the 0.8PZN-0.2PT film, while the higher binding energy peak at about 531.4 eV [marked with yellow in Fig. 3(f)] apparently originates from chemisorbed O-containing species, such as

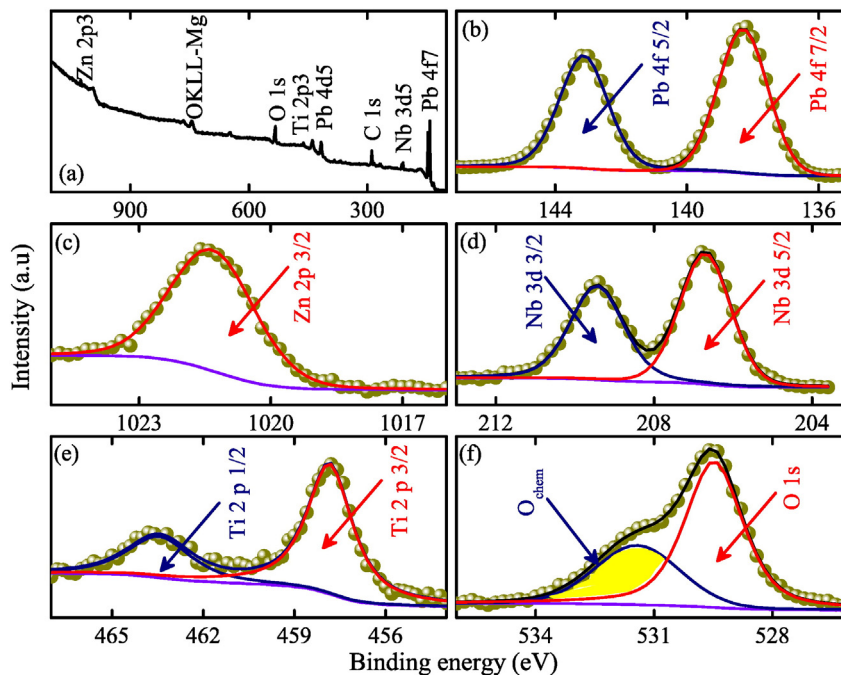


Fig. 3. XPS spectra of the (a) Pb 4f, (b) Zn 2p, (c) Nb 3d, (d) Ti 2p, and (e) O 1s regions for the 0.8PZN-0.2PT film. Note that the dotted and solid lines indicate the experimental data and fitting results, respectively. (For interpretation of the references to color in this figure, the reader is referred to the web version of this article.)

$O^{\delta-}$, $O_2^{\delta-}$, or $OH^{\delta-}$. Correspondingly, the relatively high intensity of the O_{chem} content is due to the high surface sensitivity [21].

3.3. Temperature dependent optical dispersion

To obtain the dielectric functions $\tilde{\epsilon}(E) = \epsilon_1(E) + i\epsilon_2(E)$ and other optical parameters of 0.8PZN-0.2PT films, a four-layer model [air/surface roughness layer (SRL)/0.8PZN-0.2PT/STO] was used to calculate the ellipsometric spectra of the films. One of the critical concerns for getting the accurate fitting results of the films is the selection of the substrates dispersion model and the dielectric function models. Therefore, before fitting the ellipsometric data from the 0.8PZN-0.2PT films, temperature dependent (200–600 K) dielectric spectra of the STO substrates were measured by SE in the photon energy of 1.1–6 eV. The fitting results of STO are very similar to the values reported (not shown) [22–24]. Meanwhile, note that there are many dispersion functions describing the interband transition contributions and a dielectric function derived directly from the band gap theory is suitable for the 0.8PZN-0.2PT films [25]. Fortunately, the Tauc-Lorentz (TL) model is a reasonable one to describe the dielectric dispersion of the perovskite structure materials in the NIR–UV energy region [26,27]. As we know, the standard quantum statistical mechanics or Lorentz calculation for the imaginary part of the dielectric function ϵ_2 of a collection of noninteracting atoms has been widely applied for many solid materials in the absorption region [25]. The TL dispersion model can be written as:

$$\epsilon_2(E) = \begin{cases} \frac{A_0 E_n C (E - E_g)^2}{(E^2 - E_n^2)^2 + C^2 E^2 E} \cdot \frac{1}{E}, & (E > E_g) \\ 0, & (E \leq E_g) \end{cases} \quad (1)$$

and the real part is given by the Kramers–Krönig transformation (KKT)

$$\epsilon_1(E) = \epsilon_\infty + \frac{2}{\pi} P \int_{E_g}^{\infty} \frac{\xi \epsilon_2(\xi)}{\xi^2 - E^2} d\xi \quad (2)$$

where A_0 is the transition matrix element, E_n is the peak transition energy, C is the broadening term, E_g is the band gap energy, and ϵ_∞

represents the contribution of the optical transitions at higher energies and appears as an additional fitting parameter [25,28,29]. These are mainly determinant parameters of dielectric functions. However, a good agreement was obtained between the experimental and fitted data in the entirely measured photon energy region by using the TL model in the present work (Fig. 4). It indicates that the dielectric function model can reasonably describe the interband transition of the present 0.8PZN-0.2PT films. It is worth mentioning that a SRL layer has been taken into account to reduce surface fluctuation effects caused by the high-temperature annealing [29]. The dielectric functions of the SRL layer were expressed using the Bruggeman effective medium approximation (EMA) with a mixture of film 50% and void 50% [30]. The accurate thickness of the surface roughness layer is fitted to about 5 nm, which is in agreement well with the result taken from AFM measurement. In addition, the strong coefficient correlation between the fitting parameters can be avoided by fixing film thicknesses at different temperatures [25].

As an example, the fitting procedure was carried out with the WVASE32 software package (J.A. Woollam Co., Inc.). The experimental data of the 0.8PZN-0.2PT films were fitted by the TL model, and the fitted parameters were summarized in Table 1. The experimental ellipsometric angle Ψ and Δ of the 0.8PZN-0.2PT films from 200 to 600 K are shown in Fig. 4(a) and (b). Note that the experimental ellipsometric angles Ψ and Δ move to lower energy side with increasing temperature. To clarify the temperature evolution of the photon energy E , the photon energy E were depicted in the insets 1 and 2 of Fig. 4. It can be seen that an abrupt transformation occurs at about 500 K. The temperature is designated as phase transition temperature (PTT). The experimental (dotted lines) and best-fitted (solid lines) Ψ and Δ of the 0.8PZN-0.2PT films from 200 to 600 K are shown in Fig. 4(c) and (d), respectively. There is a good agreement between the experimental and fitted data.

The real and imaginary parts of the dielectric functions at different temperature were shown in Fig. 5(a) and (b). The changes of the dielectric spectrum are explained by the charge–transfer transitions or the interband transitions [31]. The charge transfer mainly occurs between the Pb 6p, Nb 4d, Ti 3d, and O 2p or Pb 6p, Nb 4d, Ti 3d, and Zn 3d orbitals during the phase transition. The Pb–O bonding strongly affects O 2p – Ti

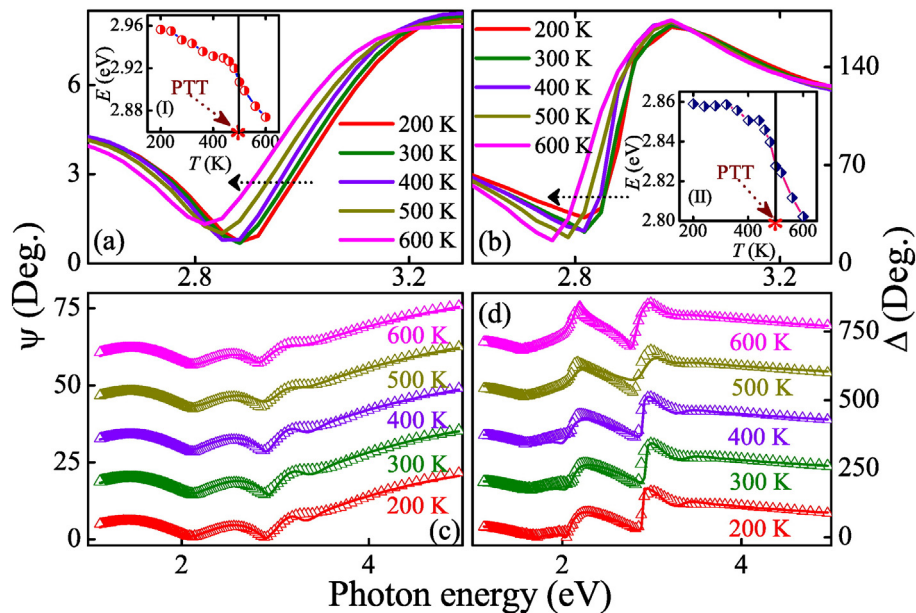


Fig. 4. Experimental ellipsometric spectra (a) Ψ and (b) Δ of the 0.8PZN-0.2PT films at the temperature from 200 K to 600 K. Note that the label (*) on behalf of the phase transition temperature (PTT). The experimental (dotted lines) and best-fitted (solid lines) ellipsometric spectra Ψ and Δ of the 0.8PZN-0.2PT films from 200 K to 600 K are shown in (c) and (d), respectively. Note that (c) and (d) Ψ spectra of the 0.8PZN-0.2PT films are vertically shifted by 14 and 170 Deg., respectively. The insets I and II show the evolution of photon energies E with temperature at $\Psi = 2$ Deg. and $\Delta = 50$ Deg., respectively.

Table 1

Dielectric function parameters using the Tauc-Lorentz oscillator dispersion for the 0.8PZN-0.2PT films determined from the simulation of ellipsometric spectra in Fig. 4. The 90% reliability of the fitting parameters is given with (\pm).

T (K)	ε_{∞}	A_0 (eV)	E_g (eV)	E_n (eV)	Γ (eV)200
200	1.91 ± 0.26	293 ± 5	3.01 ± 0.02	3.75 ± 0.01	2.55 ± 0.18
300	1.41 ± 0.15	266 ± 5	2.98 ± 0.02	3.99 ± 0.08	2.63 ± 0.12
400	1.51 ± 0.51	279 ± 5	2.92 ± 0.03	3.86 ± 0.28	2.77 ± 0.48
500	1.34 ± 0.41	265 ± 5	2.87 ± 0.05	3.93 ± 0.22	3.00 ± 0.34
600	2.38 ± 0.15	166 ± 2	2.66 ± 0.02	3.89 ± 0.06	2.67 ± 0.18

3d hybridization in the TiO_6 octahedron [32]. Correspondingly, the real part ε_1 increases with the photon energy and approaches the maximum at around 3.7 eV, which indicates a transition and ascent of absorption edge. As the photon energy increases, the imaginary part ε_2 becomes large and approaches the maximum at around 4.6 eV, suggesting a strong optical absorption. However, the real part of dielectric function decreases towards a higher energy side because of the known Van Hove singularities [25]. It should be emphasized that the maximum values of real and imaginary parts are consistent due to the KKT rule. In order to clarify the temperature evolution of the ε_1 and ε_2 , the two parameters (ε_1 and ε_2) were depicted in the insets 1 and 2 of Fig. 5 and an obvious change can be observed. With increasing temperature, the peak position of the ε_1 moves to lower energy and the absorption edge becomes narrower, which suggests a red-shift trend of the band gap E_g .

3.4. Electronic band structure

Generally, the temperature dependence of the band gap E_g from 0.8PZN-0.2PT films is sensitive to phase transition. It can be described using the Bose–Einstein model, in which the carrier–phonon coupling is taken into account [33,34]. The model can be written as:

$$E_g(T) = E_g(0) - 2a_B / \left[\exp(\Theta_B/T) - 1 \right] \quad (3)$$

here, a_B is the strength of the electron–phonon interaction and Θ_B is the characteristic temperature representing the effective phonon energy on the temperature scale [33]. The best-fitting parameters are shown in Fig. 6 and the $E_g(0)$ value can be estimated to be about 3.01 eV. From Fig. 6, we can see the band gap E_g decreases with increasing temperature. The values of E_g are similar to PZN-0.07PT crystal [35]. It is acknowledged that the decrease of the band gap E_g with temperature is caused by the electron–phonon interaction and the lattice thermal

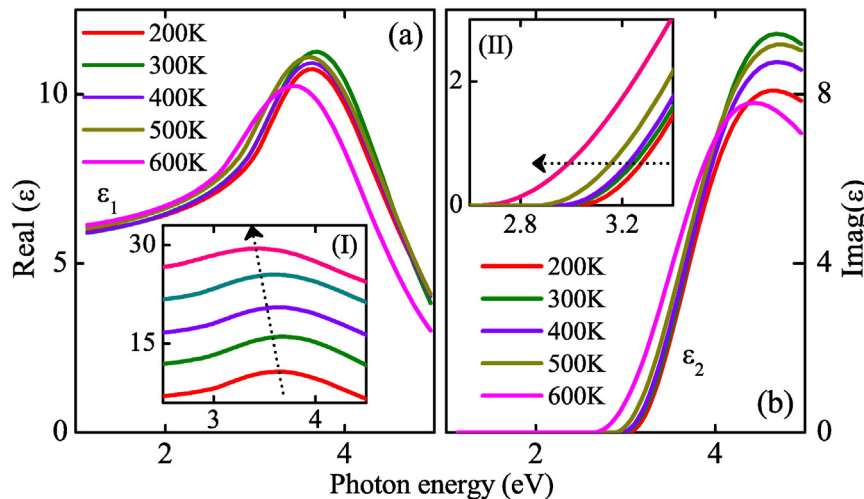


Fig. 5. Temperature dependent dielectric functions of (a) the real part ε_1 and (b) the imaginary part ε_2 . The insets I and II show ε_1 and ε_2 in the enlarged photon energy range of 2.5–4.5 eV and 2.6–3.4 eV, respectively. The ε_2 is vertically shifted up to 4.8 for each temperature.

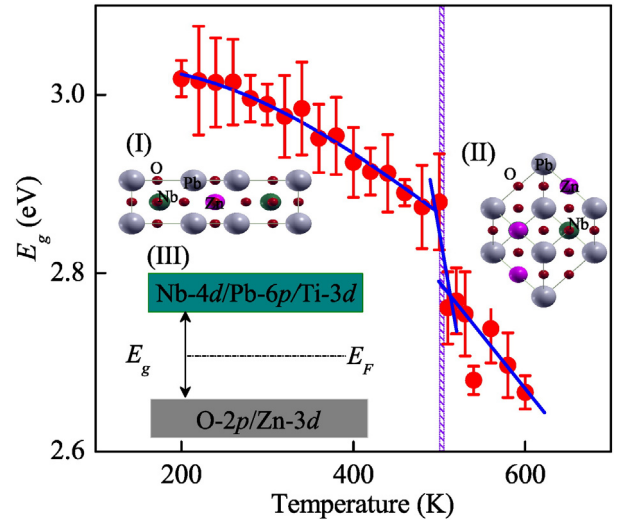


Fig. 6. Optical band gap (a) E_g as a function of temperature for the 0.8PZN-0.2PT films. Note that the shaded line indicates the phase transition point. The insets I tetragonal and II cubic structure for PZN material projected perpendicular to the different directions. The III is the schematic diagram of the electronic band structure, where the parameter E_F denotes the Fermi energy level.

expansion. With increasing temperature, the interatomic distance along the direction of their propagation can be changed by longitudinal phonon, which will further affects the lattice constant and results in the modification of energy band structure [36]. Note that the parameter E_g varies considerably and is unsatisfied the Bose–Einstein model at around 500 K, indicating that the phase transition from tetragonal ($P4mm$) to cubic ($Pm3m$) phase was occurred at this point [9]. The insets 1 and 2 of Fig. 6 show tetragonal and cubic structures of PZN material projected perpendicular to the $[001]_c$ direction, respectively [37]. Normally, PZN has small distortion with smaller polarization from cubic. However, compared with PbTiO_3 , PZN has an extremely small distortion and yet has a relatively large polarization [38].

3.5. Electronic transition mechanism

The sudden variation of the E_g from Fig. 6 is due to the distort crystal structures of 0.8PZN-0.2PT films during the phase transition with increasing temperature. It is commonly acknowledged that the modification of the lattice constant and electronic band structure can affect the

conduction band (CB) and the valence band (VB). Lattice dynamical theories indicate that the dielectric behavior as well as optical properties are primarily determined by the BO_6 octahedra because the B-site ion d orbitals and the O 2p orbitals associated with each octahedron contribute to the lower conduction bands and the upper valence bands [16]. Moreover, the first-principles calculations reveal that the CB and VB of PZN with tetragonal phase mainly consist of the O 2p and Nb 4d states, respectively. On the other hand, the CB of PZN with cubic phase is from major Nb 4d and Pb 6p states with minor contributions from O 2p states. The VB are occupied by O 2p and Zn 3d states. Pb 6p and Nb 4d states are mainly located at the higher CB region. Note that the density of states mainly consists of Pb 6p and no Zn 3d observed near the Fermi energy, which are similar to the behavior of $\text{Pb}(\text{Mg}_{1/2}\text{Nb}_{2/2})\text{O}_3$ [39]. It should be emphasized that the CB of the PT primarily consist of the Ti 3d and Pb 6p states [40]. In the process of the transition from tetragonal phase to cubic phase, the corresponding energy of absorption edges changes from 2.87 eV (at 500 K) to 2.76 eV (at 510 K). Detailed analysis shows that the electronic transitions of the absorption edges derive from three-degenerate O 2p states consisting of the two-degenerate O $2p_x$ or equivalently O $2p_y$ and the non-degenerate O $2p_z$ states. Furthermore, the variation of the E_g for cubic case is closely related to the bottom energy level of conducting Pb 6p, Nb 4d. The O 2p states become lower compared with tetragonal phase, which can be explained by the disappearance of $\text{NbO}_6/\text{ZnO}_6$ octahedrons' distortion. As a result, the renormalization of the electronic band structure, larger interatomic spacing and thermal expansion of the lattice caused by electron-phonon interaction become the dominant factors for the band gap narrowing trend with increasing temperature. The phenomena can lead to the CB downward and the VB upward. One can conclude that the above phase transition could be determined by electronic transitions from O 2p and/or Zn 3d to Nb 4d and/or Pb 6p and/or Ti 3d states, respectively. It suggests that the distorted characteristic of band gap energy is one of the critical way to identify phase transition of ferroelectric oxides.

4. Conclusions

In summary, high quality 0.8PZN-0.2PT films on STO substrates have been prepared by the sol-gel method. The XRD pattern illustrates that the preferential orientation is along the a -axis perpendicular to the substrate surface and no impurity phase is observed. The redshift trend of the electronic transformation at about 3.01 eV as a function of temperature follows the Bose-Einstein law induced by the electron-phonon interactions and lattice thermal expansion. Moreover, an abrupt transformation of the optical band gap occurred at about 500 K, which can be derived from three-degenerate O 2p states and the bottom energy level of conducting becoming lower compared with tetragonal phase. It can be associated to the disappearance of $\text{NbO}_6/\text{ZnO}_6$ octahedrons' distortion. It indicates that ferroelectric tetragonal to paraelectric cubic phase transition for 0.8PZN-0.2PT films. Meanwhile, it can be confirmed that there is an inherent relationship between optical response and structural variation for the perovskite films, which provides a valid methodology to judge the phase transition of relaxor ferroelectric materials.

Acknowledgments

The authors would like to thank Drs. Lin Sun., and Yuanyuan Zhang for constructive discussions. This work was financially supported by the Major State Basic Research Development Program of China (Grant Nos. 2011CB922200 and 2013CB922300), Natural Science Foundation of China (Grant Nos. 11374097, 61376129, and 61504156), Projects of Science and Technology Commission of Shanghai Municipality (Grant Nos. 15JC1401600, 14XD1401500, 13JC1402100, and 13JC1404200), and the Program for Professor of Special Appointment (Eastern Scholar) at Shanghai Institutions of Higher Learning.

References

- [1] H. Fu, R.E. Cohen, Polarization rotation mechanism for ultrahigh electromechanical response in single-crystal piezoelectrics, *Nature (London)* 403 (2000) 281–283.
- [2] H. You, Q.M. Zhang, Diffuse X-ray scattering study of lead magnesium niobate single crystals, *Phys. Rev. Lett.* 79 (1996) 3950–3953.
- [3] A.Y. Liu, X.J. Meng, J.Q. Xue, J.L. Sun, J. Chen, J.H. Chu, Electrical and optical properties of $\text{Pb}(\text{Mg}_{1/3}\text{Nb}_{2/3})\text{O}_3$ - PbTiO_3 thin films prepared by chemical solution deposition, *Appl. Phys. Lett.* 87 (2005) 072903.
- [4] V. Bobnar, Z. Kutnjak, R. Pirc, R. Blinc, A. Levstik, Crossover from glassy to inhomogeneous-ferroelectric nonlinear dielectric response in relaxor ferroelectrics, *Phys. Rev. Lett.* 84 (2000) 5892–5895.
- [5] J.J. Zhu, J.Z. Zhang, G.S. Xu, X.L. Zhang, Z.G. Hu, J.H. Chu, Electronic transitions and dielectric functions of relaxor ferroelectric $\text{Pb}(\text{In}_{1/2}\text{Nb}_{1/2})\text{O}_3$ - $\text{Pb}(\text{Mg}_{1/3}\text{Nb}_{2/3})\text{O}_3$ - PbTiO_3 single crystals: temperature dependent spectroscopic study, *Appl. Phys. Lett.* 104 (2014) 132903.
- [6] M. Suewattana, D.J. Singh, Electronic structure and lattice distortions in $\text{PbMg}_{1/3}\text{Nb}_{2/3}\text{O}_3$ studied with density functional theory using the linearized augmented plane-wave method, *Phys. Rev. B* 73 (2006) 224105.
- [7] B. Mihailova, B. Maier, C. Paulmann, T. Malcherek, J. Ihringer, M. Gospodinov, R. Stosch, B. Güttler, U. Bismayer, High-temperature structural transformations in the relaxor ferroelectrics $\text{PbSc}_{0.5}\text{Ta}_{0.5}\text{O}_3$ and $\text{Pb}_{0.78}\text{Ba}_{0.22}\text{Sc}_{0.5}\text{Ta}_{0.5}\text{O}_3$, *Phys. Rev. B* 77 (2008) 174106.
- [8] S. Kim, I.S. Yang, Raman study of an electric-field-induced phase transition in $\text{Pb}(\text{Zn}_{1/3}\text{Nb}_{2/3})\text{O}_3$ -8% PbTiO_3 , *Phys. Rev. B* 64 (2001) 094105.
- [9] D. La-Orautapong, B. Noheda, Z.G. Ye, P.M. Gehring, J. Toulouse, D.E. Cox, G. Shirane, Phase diagram of the relaxor ferroelectric $(1-x)\text{Pb}(\text{Zn}_{1/3}\text{Nb}_{2/3})\text{O}_3$ - $x\text{PbTiO}_3$, *Phys. Rev. B* 65 (2002) 144101.
- [10] K.K. Mishra, A.K. Arora, S.N. Tripathy, D. Pradhan, Dielectric and polarized Raman spectroscopic studies on 0.85 $\text{Pb}(\text{Zn}_{1/3}\text{Nb}_{2/3})\text{O}_3$ -0.15 PbTiO_3 single crystal, *J. Appl. Phys.* 112 (2012) 073521.
- [11] J. Qian, J.Y. Xu, M. Jin, H. Shen, The influence of domain structures and phase transition on transmittance of PZN-PT ferroelectric crystal, *J. Phys. D: Appl. Phys.* 47 (2014) 405501.
- [12] B.G. Kim, S.M. Cho, T.Y. Kim, H.M. Jang, Giant dielectric permittivity observed in Pb-based perovskite ferroelectrics, *Phys. Rev. Lett.* 86 (2001) 3404–3406.
- [13] B. Noheda, D.E. Cox, G. Shirane, S.E. Park, L.E. Cross, Z. Zhong, Polarization rotation via a monoclinic phase in the piezoelectric 92% $\text{Pb}(\text{Zn}_{1/3}\text{Nb}_{2/3})\text{O}_3$ -8% PbTiO_3 , *Phys. Rev. Lett.* 86 (2001) 3891–3894.
- [14] W. Ren, S.-F. Liu, B.K. Mukherjee, Piezoelectric properties and phase transitions of (001)-oriented $\text{Pb}(\text{Zn}_{1/3}\text{Nb}_{2/3})\text{O}_3$ - PbTiO_3 single crystals, *Appl. Phys. Lett.* 80 (2002) 3174–3176.
- [15] D.S. Paik, S.E. Park, S. Wada, S.F. Liu, T.R. Shrout, E-field induced phase transition in (001)-oriented rhombohedral 0.92 $\text{Pb}(\text{Zn}_{1/3}\text{Nb}_{2/3})\text{O}_3$ -0.08 PbTiO_3 crystals, *J. Appl. Phys.* 85 (1999) 1080–1083.
- [16] M. DiDomenico Jr, S.H. Wemple, Oxygen-octahedra ferroelectrics. I. Theory of Electro-optical and nonlinear optical effects, *J. Appl. Phys.* 40 (1969) 720–734.
- [17] S.H. Wemple, M. DiDomenico Jr, Oxygen-octahedra ferroelectrics. II. Electro-optical and nonlinear-optical device applications, *J. Appl. Phys.* 40 (1969) 735–752.
- [18] C.Q. Li, A.Y. Liu, J.Q. Shi, Y.F. Ruan, J.H. Chu, X.D. Zhang, Structure and dielectric properties of 80% $\text{Pb}(\text{Zn}_{1/3}\text{Nb}_{2/3})\text{O}_3$ -20% PbTiO_3 thin films prepared by modified sol-gel process, *J. Sol-Gel Sci. Technol.* 60 (2011) 164–169.
- [19] K.Y. Chan, W.S. Tsang, C.L. Mak, K.H. Wong, Effects of composition of PbTiO_3 on optical properties of $(1-x)\text{Pb}(\text{Zn}_{1/3}\text{Nb}_{2/3})\text{O}_3$ - $x\text{PbTiO}_3$ thin films, *Phys. Rev. B* 69 (2004) 144111.
- [20] M. Wu, H.Y. Huang, W.Y. Chu, L.Q. Guo, L.J. Qiao, J.Y. Xu, T.Y. Zhang, Tuning the ferroelectric and piezoelectric properties of 0.91 $\text{Pb}(\text{Zn}_{1/3}\text{Nb}_{2/3})\text{O}_3$ -0.09 PbTiO_3 single crystals and lead zirconate titanate ceramics by doping hydrogen, *J. Phys. Chem. C* 114 (2010) 9955–9960.
- [21] A. Kolmakov, S. Potluri, A. Barinov, T.O. Mentis, L. Gregoratti, M.A. Nino, A. Locatelli, M. Kiskinova, Spectromicroscopy for addressing the surface and electron transport properties of individual 1-D nanostructures and their networks, *ACS Nano* 2 (2008) 1993–2000.
- [22] M. Rössle, C.N. Wang, P. Marsik, M. Yazdi-Rizi, K.W. Kim, A. Dubroka, I. Marozau, C.W. Schneider, D. Baeriswyl, C. Bernhard, Optical probe of ferroelectric order in bulk and thin-film perovskite titanates, *Phys. Rev. B* 88 (2013) 104110.
- [23] K.V. Benthem, C. Elsaesser, R.H. French, Bulk electronic structure of SrTiO_3 : experiment and theory, *J. Appl. Phys.* 90 (2001) 6156–6164.
- [24] M. Cardona, Optical Properties and Band Structure of SrTiO_3 and BaTiO_3 , *Phys. Rev. B* 140 (1965) A651–A655.
- [25] S. Zhang, J.Z. Zhang, M.J. Han, Y.W. Li, Z.G. Hu, J.H. Chu, Temperature dependent near infrared ultraviolet range dielectric functions of nanocrystalline $(\text{Na}_{0.5}\text{Bi}_{0.5})_{1-x}\text{Ce}_x(\text{Ti}_{0.99}\text{Fe}_{0.01})\text{O}_3$ films, *Appl. Phys. Lett.* 104 (2014) 041106.
- [26] S.B. Anooz, J. Schwarzkopf, R. Dirsyte, E. Ehrstein, P. Petrik, A. Kwasniewski, G. Wagner, R. Fornari, Spectroscopic ellipsometry studies on the optical constants of $\text{Bi}_4\text{Ti}_3\text{O}_{12}$ - $x\text{Na}$ thin films grown by metal-organic chemical vapor deposition, *Thin Solid Films* 519 (2011) 3782–3788.
- [27] Y.J. Cho, N.V. Nguyen, C.A. Richter, J.R. Ehrstein, B.H. Lee, J.C. Lee, Spectroscopic ellipsometry characterization of high- k dielectric HfO_2 thin films and the high-temperature annealing effects on their optical properties, *Appl. Phys. Lett.* 80 (2002) 1249–1251.
- [28] Z.G. Hu, J.H. Ma, Z.M. Huang, Y.N. Wu, G.S. Wang, J.H. Chu, Dielectric functions of ferroelectric $\text{Bi}_{3.25}\text{La}_{0.75}\text{Ti}_3\text{O}_{12}$ thin films on Si(100) substrates, *Appl. Phys. Lett.* 83 (2003) 3686–3688.

- [29] J. Kvietkova, B. Daniel, M. Hetterich, M. Schubert, D. Spemann, D. Litvinov, D. Gerthsen, Near-band-gap dielectric function of $\text{Zn}_{1-x}\text{Mn}_x\text{Se}$ thin films determined by spectroscopic ellipsometry, *Phys. Rev. B* 70 (2004) 045316.
- [30] Z.G. Hu, P. Hess, Optical constants and thermo-optic coefficients of nanocrystalline diamond films at 30–500°C, *Appl. Phys. Lett.* 89 (2006) 081906.
- [31] S.G. Choi, H.T. Yi, S.W. Cheong, J.N. Hifiker, R. France, A.G. Norman, Optical anisotropy and charge-transfer transition energies in BiFeO_3 from 1.0 to 5.5 eV, *Phys. Rev. B* 83 (2011) 100101.
- [32] J.C. Jan, H.M. Tsai, C.W. Pao, J.W. Chiou, K. Asokan, K.P.K. Kumar, W.F. Pong, Y.H. Tang, M.H. Tsai, S.Y. Kuo, W.F. Hsieh, Direct experimental evidence of hybridization of Pb states with O 2p states in ferroelectric perovskite oxides, *Appl. Phys. Lett.* 87 (2005) 012103.
- [33] M. Beaudoin, A.J.G. DeVries, S.R. Johnson, H. Laman, T. Tiedje, Optical absorption edge of semi-insulating GaAs and InP at high temperatures, *Appl. Phys. Lett.* 70 (1997) 3540–3542.
- [34] M.J. Han, K. Jiang, J.Z. Zhang, Y.W. Li, Z.G. Hu, J.H. Chu, Temperature dependent phonon evolutions and optical properties of highly c-axis oriented CuGaO_2 semiconductor films grown by the sol-gel method, *Appl. Phys. Lett.* 99 (2011) 131104.
- [35] E.W. Sun, R. Zhang, Z. Wang, D.P. Xu, L. Li, W.W. Cao, Optical interband transitions in relaxor-based ferroelectric $0.93\text{Pb}(\text{Zn}_{1/3}\text{Nb}_{2/3})\text{O}_3$ - 0.07PbTiO_3 single crystal, *J. Appl. Phys.* 107 (2010) 113532.
- [36] S.A. Lourenco, I.F.L. Dias, J.L. Duarte, E. Laureto, E.A. Mensess, J.R. Leite, I. Mazzaro, Temperature dependence of optical transitions in AlGaAs, *J. Appl. Phys.* 89 (2001) 6159–6164.
- [37] J.Z. Zhang, W.Y. Tong, J.J. Zhu, J.Y. Xu, Z.H. Duan, L.P. Xu, Z.G. Hu, C.G. Duan, X.J. Meng, Z.Q. Zhu, J.H. Chu, Temperature-dependent lattice dynamics and electronic transitions in $0.93\text{Pb}(\text{Zn}_{1/3}\text{Nb}_{2/3})\text{O}_3$ - 0.07PbTiO_3 single crystals: experiment and theory, *Phys. Rev. B* 91 (2015) 085201.
- [38] E.H. Kisi, J.S. Forrester, K.S. Knight, $\text{PbZn}_{1/3}\text{Nb}_{2/3}\text{O}_3$ at 4.2 and 295 K, *Acta Crystallogr. Sect. C* 62 (2006) i46–i48.
- [39] M. Suewattana, D.J. Singh, Electronic structure and lattice distortions in $\text{PbMg}_{1/3}\text{Nb}_{2/3}\text{O}_3$ studied with density functional theory using the linearized augmented plane-wave method, *Phys. Rev. B* 73 (2006) 224105.
- [40] M. Kitamura, H. Chen, Electronic structure calculations of perovskite-type oxides using the self-consistent-charge extended Hückel tight-binding method, *Ferroelectrics* 210 (1998) 13–29.